

Electronic Supplementary Information

for

Impact of dehydration and mechanical amorphization on the magnetic properties of Ni(II)-MOF-74

by

Senada Muratović,^a Bahar Karadeniz,^a Tomislav Stolar,^a Stipe Lukin,^a Ivan Halasz,^a Mirta Herak,^b Gregor Mali,^c Yulia Krupskaya,^d Vladislav Kataev,^d
Dijana Žilić*^a and Krunoslav Užarević*^a

^a Ruđer Bošković Institute, Bijenička cesta 54, 10000 Zagreb, Croatia.

^b Institute of Physics, Bijenička cesta 46, 10000 Zagreb, Croatia.

^c National Institute of Chemistry, Hajdrihova 19, SI-1001 Ljubljana, Slovenia.

^d Leibniz IFW Dresden, Helmholtzstrasse 20, D-01069 Dresden, Germany.

E-mail: dijana.zilic@irb.hr, krunoslav.uzarevic@irb.hr

Contents

S1 Experimental	4
S1.1 Synthesis	4
S1.2 Dehydration	4
S1.3 Synthesis and desolvation of Zn-MOF-74	4
S1.4 Amorphization	4
S1.5 In situ monitoring of milling reactions	4
S1.6 PXRD	5
S1.7 Magnetization measurements	5
S1.8 ESR spectroscopy	5
S1.9 IR spectroscopy	5
S1.10 TGA	6
S1.11 Scanning electron microscopy (SEM)	6
S1.12 Solid state NMR spectroscopy	6
S2 Simulation of ESR spectra of Ni-INT	6
S3 Figures	7

List of Figures

S1	PXRD data for Ni-MOF-74 (green), Ni-INT (blue), calculated Ni-MOF-74 (black, CCDC code LEJRIC) and calculated Ni-INT (red) ¹	7
S2	PXRD data for Ni-MOF-74 (black), <i>deh</i> -Ni-MOF-74 (blue), <i>am</i> -Ni-MOF-74 (brown) and calculated Ni-MOF-74 (red, CCDC code LEJRIC).	8
S3	PXRD data for Ni-MOF-74 (green), compared to different amorphous Ni-MOF-74 samples after 90 minutes milling in a ball mill. All samples show no Bragg reflections. Small differences in PXRD of sample d is due to different collection parameters (low-angle knife positioned before the sample).	8
S4	FTIR-ATR data for different amorphous Ni-MOF-74 samples after 90 minutes milling in a ball mill.	9
S5	Time-resolved PXRD data for Ni-MOF-74 (green) sampled after different milling periods. The continuation of milling gradually diminishes crystallinity of the sample.	9
S6	SEM images of a) Ni-MOF-74, b) <i>deh</i> -Ni-MOF-74 and c) <i>am</i> -Ni-MOF-74 recorded under the same conditions.	10
S7	Field dependence of the magnetization, M vs H , of the Ni-INT complex at $T = 1.8$ K.	10
S8	Temperature dependencies of the static susceptibility $\chi(T)$ (purple symbols) and the inverse susceptibility $\chi^{-1}(T)$ (cyan symbols) of the Ni-INT complex in a magnetic field of $\mu_0 H = 1$ T. A solid line is the fit on Curie-Weiss law with the fitting parameter given in the inset.	11
S9	Temperature dependence of X-band ESR spectra of Ni-INT complex. ESR peaks marked by asterisks are the cavity signals. The simulated spectrum at $T = 5$ K with parameter given in Table S1 is also shown.	11

S10	Field dependence of magnetization of <i>am</i> -Ni-MOF-74 at $T = 1.8$ K plotted with Brillouin function.	12
S11	Temperature dependence of X-band ESR spectra of two <i>am</i> -Ni-MOF-74 samples showing that the compound is ESR silent. Sharp peaks marked by asterisks are the ESR cavity signals. Sloping baselines for Sample 2 are connected with temperature stabilization.	12
S12	The comparison of HF-ESR spectra of all investigated compounds recorded at the same frequency (321 GHz) and the same temperature (3 K). For <i>am</i> -Ni-MOF-74, HF-ESR spectra of two different samples are shown.	13
S13	Frequency <i>vs</i> resonance field dependencies $\nu(B)$ of the prominent spectral point, together with the selected spectra of Ni-MOF-74, <i>deh</i> -Ni-MOF-74 and <i>am</i> -Ni-MOF-74 compounds at $T = 60$ K.	13
S14	^{13}C MAS NMR spectrum of Ni-MOF-74 and its decomposition into several contributions. On top, the experimental spectrum (blue) is compared to the modelled one (thin red). The experimental spectrum is modelled by a sum of seven spinning sideband patterns, which can, according to the isotropic shifts, be divided into four significantly distinct contributions. Isotropic shifts for the sideband patterns with narrow lines are listed; bands at these isotropic shifts (centerbands) are marked by black vertical lines. The experimental spectrum presented in this figure is a sum of three subspectra, which were recorded using three different irradiation frequencies. The irradiation frequency was increased in a step of $3 \cdot \nu_R$, where ν_R is MAS frequency of 38 kHz	14
S15	^{13}C MAS NMR spectrum of <i>am</i> -Ni-MOF-74, and ^1H - ^{13}C CPMAS NMR spectra of <i>am</i> -Zn-MOF-74 and Zn-MOF-74	15
S16	TGA data of <i>am</i> -Ni-MOF-74.	16
S17	Comparison of <i>ex situ</i> Raman spectra of crystalline and amorphous Ni-MOF-74. Raman bands undergoing major changes are highlighted.	16
S18	<i>In situ</i> monitoring a) PXRD and b) Raman data for recrystallization of Zn-MOF-74 by LAG(MeOH).	17
S19	PXRD data for recrystallization of <i>am</i> -Ni-MOF-74 by LAG with MeOH (red) and H ₂ O (blue) compared to the PXRD of crystalline Ni-MOF-74 (black)	17
S20	PXRD data for recrystallization of <i>am</i> -Ni-MOF-74 by accelerated aging (AA) (10 days at 45°C) in the atmosphere of MeOH (red) and H ₂ O (blue) compared to the PXRD of crystalline Ni-MOF-74 (black)	18

List of Tables

S1	The spin-Hamiltonian parameters defined by relations S1–S4 used for the simulation HF-ESR spectra of Ni-INT	7
----	---	---

S1 Experimental

S1.1 Synthesis

Synthesis of Ni-INT and Ni-MOF-74 was prepared according to literature method.²

For the synthesis of Ni-INT, 5 mL aqueous solution of Ni(OAc)₂·4H₂O (100 mg, 0.40 mmol) was added dropwise to the aqueous suspension of 2,5-dihydroxy terephthalic acid (DHTA) (79.62 mg, 0.40 mmol) (10 mL) at 60°C. After the addition was completed green precipitate was formed and the reaction was gently stirred for 10 minutes to complete the precipitation and left to cool down to the RT. A light green powder was filtered, washed with H₂O (3x2 mL) and air dried.

For the synthesis of Ni-MOF-74, to 5 mL aqueous (100°C) suspension of DHTA (79.62 mg, 0.40 mmol), 5 mL aqueous solution (100°C) of Ni(OAc)₂·4H₂O (195 mg, 0.78 mmol) was dropped and green solution was obtained. After 10 minutes of refluxing yellow precipitate was observed and reaction mixture was further refluxed for 1 h. Yellow product was filtered, washed with H₂O (3x2 mL) and air dried.

S1.2 Dehydration

Ni-MOF-74 was first activated with acetone by soaking the sample in acetone for 3 days and changing the solvent three times in a day. The sample was filtrated and placed in a vacuum oven for 24 h at 90°C. Desolvated sample was then transferred to a Schlenk system in ESR tube to be purged and kept under argon atmosphere and finally submitted for ESR and VSM magnetization measurements.

S1.3 Synthesis and desolvation of Zn-MOF-74

Mechanochemical synthesis of Zn-MOF-74 was achieved by milling 225 mg of ZnO (2.76 mmol) with 275 mg of DHTA (1.39 mmol) and using 312 μ L of MeOH as liquid additive. Milling was performed in a mixer mill (InSolidoTechnologies) using 14 mL PMMA jar, one 2.7 g tungsten carbide ball as milling media, at 30 Hz operating frequency and 3 h milling time. Desolvated Zn-MOF-74 was prepared by keeping the sample at 150 °C in an oven for a period of 24h.

S1.4 Amorphization

Dehydrated Ni-MOF-74 and Zn-MOF-74 were placed into a virgin poly(methyl methacrylate) (PMMA) jar with a zirconium ball (4 mg) and milled at IST-500 model mixer mill at 30 Hz for 2 h. Amorphous samples were analyzed by PXRD.

S1.5 In situ monitoring of milling reactions

Monitoring of mechanochemical reactions was performed ID15A experimental hutch at the European Synchrotron and Radiation Facility (ESRF) in Grenoble according to the standard methodology.^{3,4} In each experiment, we weighed 200 mg of MOF-74 material in a 14 mL transparent reaction jar made from polymethyl methacrylate (PMMA), and as milling media, we used two tungsten carbide balls each with the diameter of 7 mm and the mass of 2.9 g. X-ray beam ($\lambda = 0.1797 \text{ \AA}$)

was positioned to hit the bottom of the jar, and diffracted data was collected on a Dectris Pilatus CdTe 2M detector. We performed the integration of raw diffraction data with the ESRF in house MATLAB script. The time between consecutive diffraction patterns was 5 s. For Raman spectroscopy monitoring, we used modular Raman system equipped with OceanOptics Maya2000Pro spectrometer having a resolution of 4 cm^{-1} coupled with the B&W-Tek fiber-optic Raman BAC102 probe, and the PD-LD (now Necsel) Blue-Box Raman laser with the 785 nm extinction wavelength. We positioned the Raman probe perpendicular to the X-ray beam such that the laser beam hit approximately the same portion of material inside of the jar. The time resolution of Raman spectra was 10 s, while details about the subtraction of the Raman spectrum of PMMA jar from experimental spectra have already been described elsewhere.^{3,4} Starting and ending of milling was done remotely from the control room, as well as a simultaneous collection of PXR and Raman data, that both started with 2 seconds delay after the start of milling.

S1.6 PXR

PXR analysis was performed using Panalytical Aeris Research tabletop diffractometer equipped with Ni-filtered CuK radiation and the X-ray tube operating at 7.5 mA and 40 kV, using zero background sample holder, Bragg Brentano geometry.

S1.7 Magnetization measurements

Field- and temperature- dependencies of the static magnetization were measured in the temperature range 1.8–300 K and in magnetic fields up to 7 T using a commercial SQUID (superconducting quantum interference device) VSM (vibrating sample magnetometer) from Quantum Design. The powder samples were cooled down from the room down to the lowest temperature without magnetic field, then measured $M(H)$ from 0 to 7 T and back to 0 T, then applied field of 1 T and measured $M(T)$ upon heating.

S1.8 ESR spectroscopy

X-band ESR experiments were obtained using Bruker Eleksys 580 FT/CW spectrometer. The spectra were recorded from room down to liquid helium temperature with a magnetic field modulation amplitude of 0.5 mT and frequency of 100 kHz. HF-ESR experiments were carried out with a home-made spectrometer based on Vector Network Analyzer (PNA-X from Keysight Technologies). The HF-ESR spectrometer uses a 16 T magnetocryostat (Oxford Instruments Ltd.). For more details, see Ref.⁵. The spectra of powder samples were recorded in the temperature range 3–150 K, at several selected frequencies up to 321 GHz.

S1.9 IR spectroscopy

FTIR-ATR measurements were conducted using Perkin-Elmer Spectrum Two spectrometer with diamond cell. The data was collected in the range of 4400 cm^{-1} to 450 cm^{-1} , resolution of 4 cm^{-1} . Spectrum software (version 10.5.3.738, 2016) was used for data processing.

S1.10 TGA

TGA was performed using Shimadzu DTG-60H in the air atmosphere, in temperature range 30–800°C with 10°C/min heating rate.

S1.11 Scanning electron microscopy (SEM)

Micrographs of MOF-74 samples were collected with JEOL JSM-7000F Field Emission Scanning Electron Microscope. MOFs were not coated with conductive layer.

S1.12 Solid state NMR spectroscopy

^{13}C magic-angle spinning (MAS) and ^1H – ^{13}C cross-polarization (CP) MAS NMR spectra were recorded on a 600 MHz Varian VNMRS spectrometer equipped with 1.6 mm HXY Varian MAS probe. For each Ni-containing sample two spectra were recorded, one at MAS frequency of 38 kHz and one at MAS frequency of 40 kHz; this enabled identification of centerbands in the spinning sidebands patterns and thus the determination of isotropic shifts of the contributions to the spectra. The spectra were obtained with Hahn echo sequence. Durations of 90- and 180-degree pulses were 2 μs and 4 μs , respectively, and the inter-pulse delay was equal to one rotation period. Repetition delay between consecutive scans was 62.5 ms and the number of scans varied between 100 000 and 800 000. ^1H – ^{13}C CPMAS NMR spectra of Zn-containing samples were recorded at MAS frequency of 32 kHz using ramp during 5 ms CP block and high-power XiX proton decoupling during acquisition. Repetition delay was 2 s for the crystalline sample and 4 s for the amorphous sample; number of scans was 3200. All ^{13}C shifts were reported relative to the position of the ^{13}C signal of tetramethylsilane (TMS).

S2 Simulation of ESR spectra of Ni-INT

In order to simulate spectra of non-isolated Ni(II) ions, we assumed the following expanded form of the spin-Hamiltonian:

$$\mathbf{H} = \sum_i [\mathbf{H}_{EZI}(i) + \mathbf{H}_{ZFI}(i)] + \sum_i \sum_{i>j} \mathbf{H}_{EEI}(i, j) \quad (\text{S1})$$

where the first and the second term describe electron Zeeman interaction and interaction with the ligand field (zero-field splitting, ZFS), respectively, of nickel(II) electron spin i while the third term presents spin-spin interaction between electron spins i and j .⁶ Three terms in relation S1 are defined as following:

$$\mathbf{H}_{EZI} = \mu_B \mathbf{B} \cdot \mathbf{g} \cdot \mathbf{S}, \quad (\text{S2})$$

$$\mathbf{H}_{ZFI}/h = D[S_z^2 - S(S+1)/3] + E(S_+^2 - S_-^2), \quad (\text{S3})$$

$$\mathbf{H}_{EEI}/h = -\mathbf{S}_i \cdot \mathbf{J} \cdot \mathbf{S}_j, \quad (\text{S4})$$

where \mathbf{B} is the applied magnetic field, \mathbf{g} is \mathbf{g} -tensor, and D and E are axial and rhombic ZFS-parameter, respectively.⁶ The \mathbf{J} tensor describes the total interaction between spins: isotropic, antisymmetric and symmetric interactions.⁶ The powder-averaged spectra are simulated by using the

EasySpin software.^{6,7} For the simulation, g -tensor of nickel(II) is approximated with an isotropic g -value in agreement with the values that could be found in literature.^{8,9} The spin-spin interaction is also described by an isotropic parameter J between two nickel ions, while hyperfine interaction of electron spin and nucleus spin is neglected. The parameters used for the simulation are given in Table S1. Negative values of the axial ZFS parameter D points to the easy-axis type of magnetic anisotropy of Ni(II) ion while the sign (plus or minus) of the rhombic ZFS parameter E does not have physical meaning.¹⁰

Table S1: The spin-Hamiltonian parameters defined by relations S1–S4 used for the simulation HF-ESR spectra of Ni-INT

Compound	g	D	$ E $	J
Ni-INT	2.2	-2.24 cm^{-1}	0.33 cm^{-1}	-0.51 cm^{-1}

S3 Figures

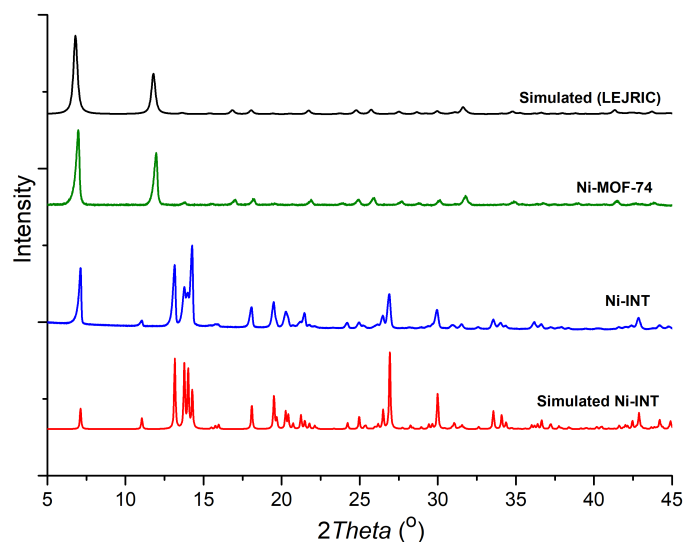


Figure S1: PXRD data for Ni-MOF-74 (green), Ni-INT (blue), calculated Ni-MOF-74 (black, CCDC code LEJRIC) and calculated Ni-INT (red)¹.

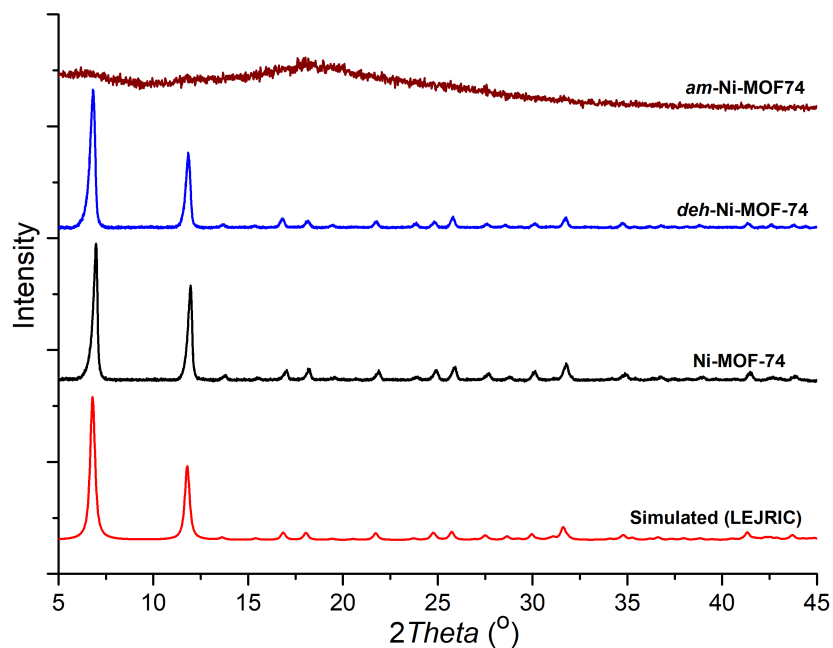


Figure S2: PXR D data for Ni-MOF-74 (black), *deh*-Ni-MOF-74 (blue), *am*-Ni-MOF-74 (brown) and calculated Ni-MOF-74 (red, CCDC code LEJRIC).

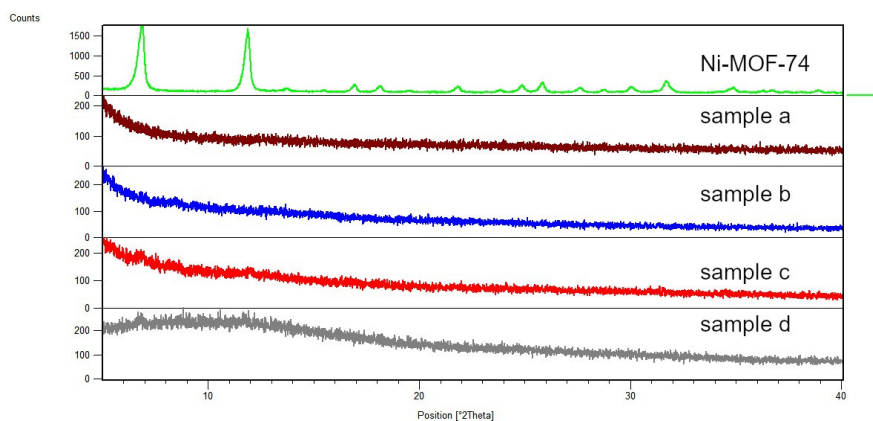


Figure S3: PXR D data for Ni-MOF-74 (green), compared to different amorphous Ni-MOF-74 samples after 90 minutes milling in a ball mill. All samples show no Bragg reflections. Small differences in PXR D of sample d is due to different collection parameters (low-angle knife positioned before the sample).

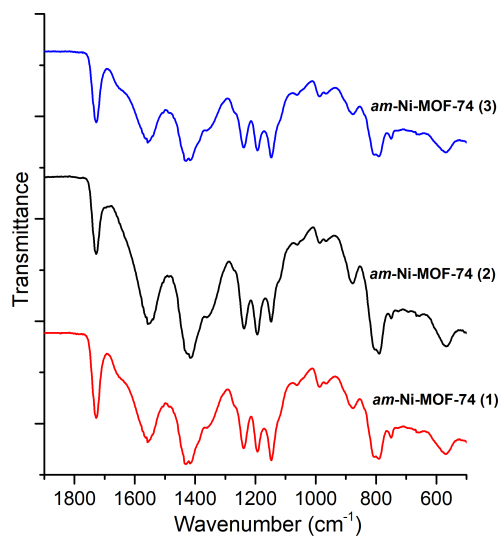


Figure S4: FTIR-ATR data for different amorphous Ni-MOF-74 samples after 90 minutes milling in a ball mill.

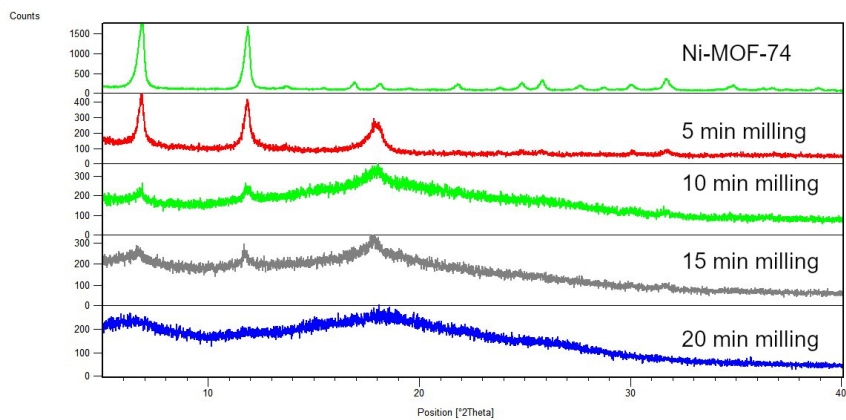


Figure S5: Time-resolved PXRD data for Ni-MOF-74 (green) sampled after different milling periods. The continuation of milling gradually diminishes crystallinity of the sample.

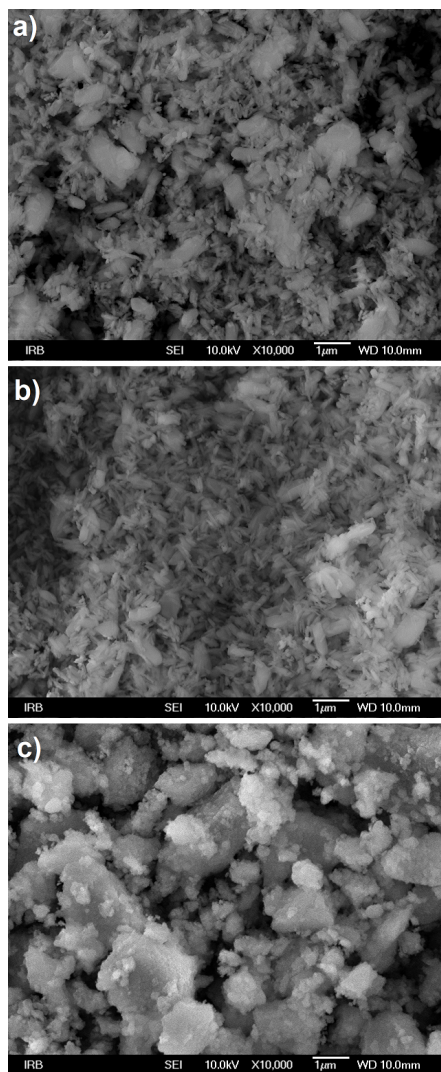


Figure S6: SEM images of a) Ni-MOF-74, b) *deh*-Ni-MOF-74 and c) *am*-Ni-MOF-74 recorded under the same conditions.

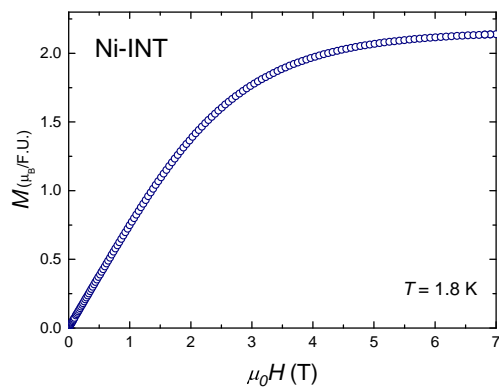


Figure S7: Field dependence of the magnetization, M vs H , of the Ni-INT complex at $T = 1.8$ K.

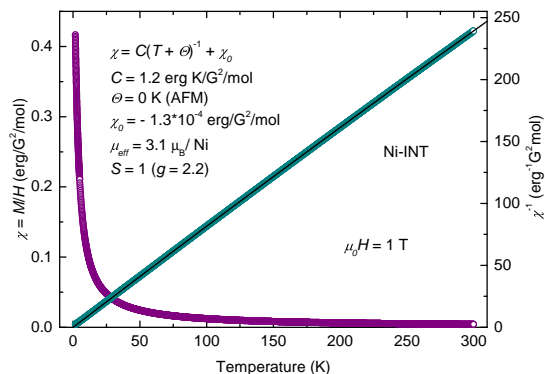


Figure S8: Temperature dependencies of the static susceptibility $\chi(T)$ (purple symbols) and the inverse susceptibility $\chi^{-1}(T)$ (cyan symbols) of the Ni-INT complex in a magnetic field of $\mu_0 H = 1$ T. A solid line is the fit on Curie-Weiss law with the fitting parameter given in the inset.

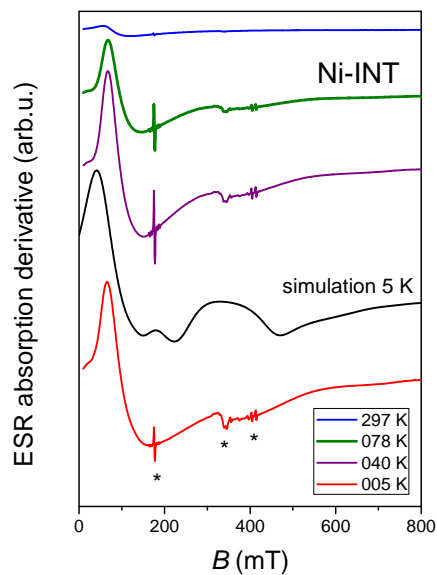


Figure S9: Temperature dependence of X-band ESR spectra of Ni-INT complex. ESR peaks marked by asterisks are the cavity signals. The simulated spectrum at $T = 5$ K with parameter given in Table S1 is also shown.

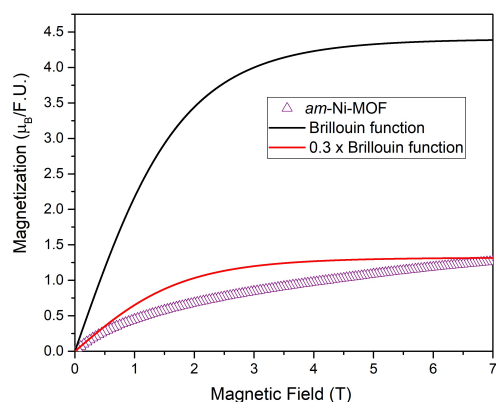


Figure S10: Field dependence of magnetization of *am*-Ni-MOF-74 at $T = 1.8$ K plotted with Brillouin function.

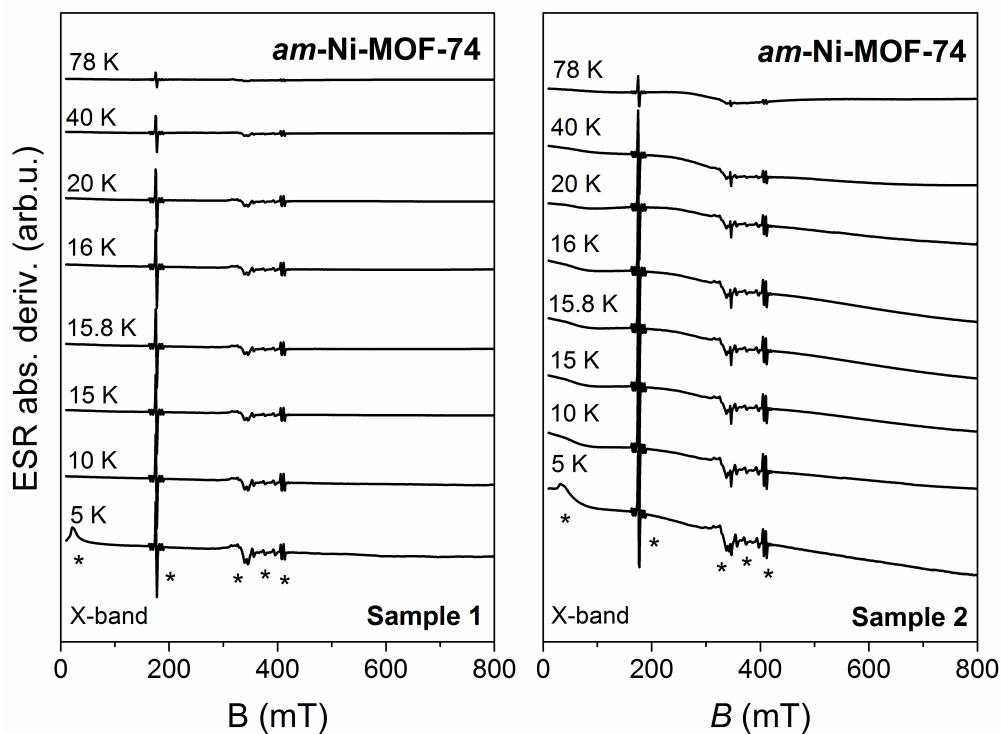


Figure S11: Temperature dependence of X-band ESR spectra of two *am*-Ni-MOF-74 samples showing that the compound is ESR silent. Sharp peaks marked by asterisks are the ESR cavity signals. Sloping baselines for Sample 2 are connected with temperature stabilization.

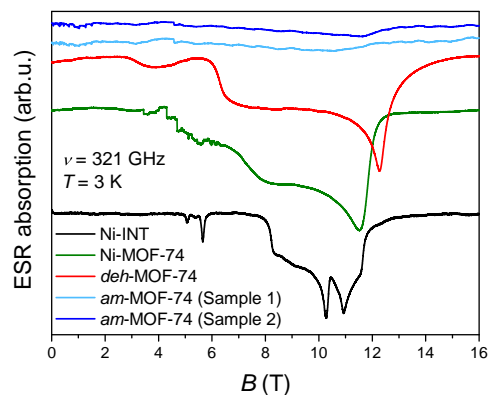


Figure S12: The comparison of HF-ESR spectra of all investigated compounds recorded at the same frequency (321 GHz) and the same temperature (3 K). For *am*-Ni-MOF-74, HF-ESR spectra of two different samples are shown.

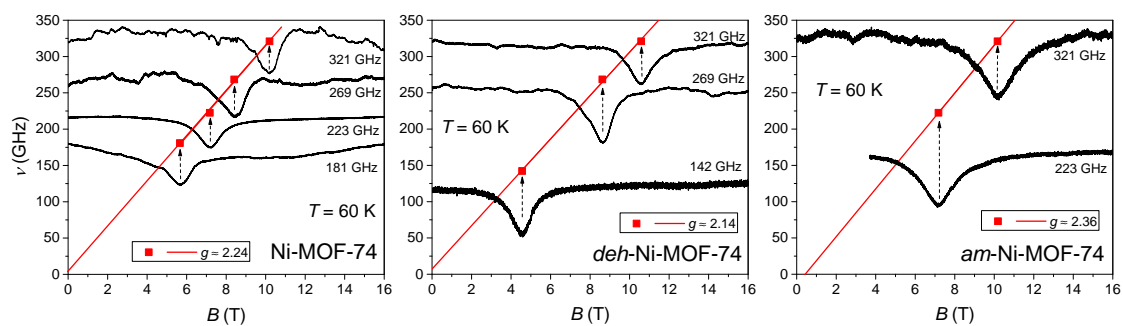


Figure S13: Frequency ν vs resonance field dependencies $\nu(B)$ of the prominent spectral point, together with the selected spectra of Ni-MOF-74, *deh*-Ni-MOF-74 and *am*-Ni-MOF-74 compounds at $T = 60$ K.

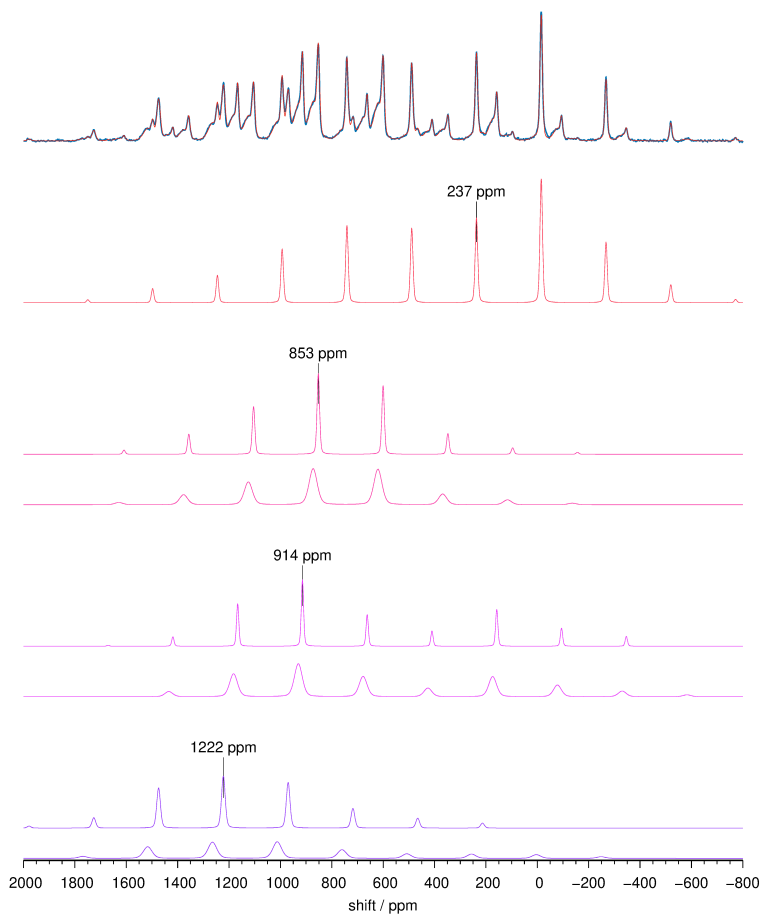


Figure S14: ^{13}C MAS NMR spectrum of Ni-MOF-74 and its decomposition into several contributions. On top, the experimental spectrum (blue) is compared to the modelled one (thin red). The experimental spectrum is modelled by a sum of seven spinning sideband patterns, which can, according to the isotropic shifts, be divided into four significantly distinct contributions. Isotropic shifts for the sideband patterns with narrow lines are listed; bands at these isotropic shifts (center-bands) are marked by black vertical lines. The experimental spectrum presented in this figure is a sum of three subspectra, which were recorded using three different irradiation frequencies. The irradiation frequency was increased in a step of $3 \cdot \nu_R$, where ν_R is MAS frequency of 38 kHz

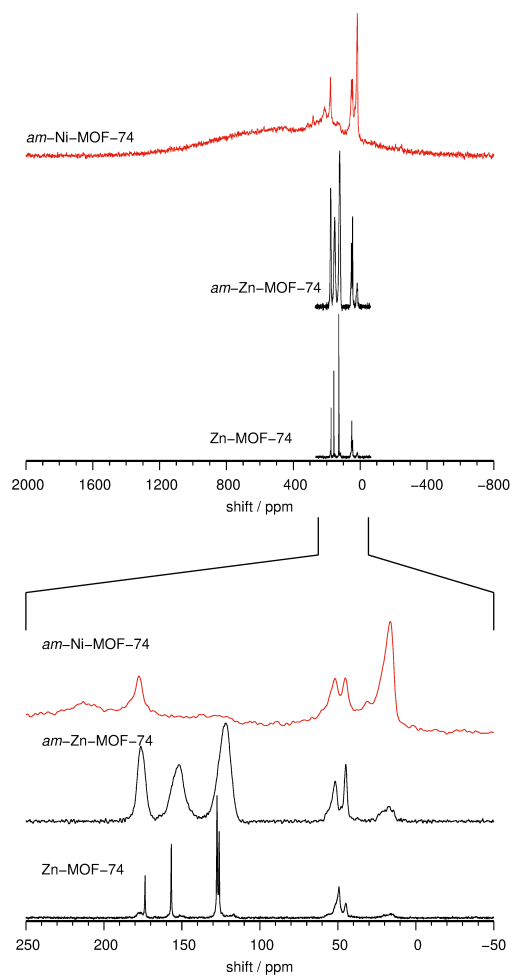


Figure S15: ^{13}C MAS NMR spectrum of *am*-Ni-MOF-74, and ^1H - ^{13}C CPMAS NMR spectra of *am*-Zn-MOF-74 and Zn-MOF-74

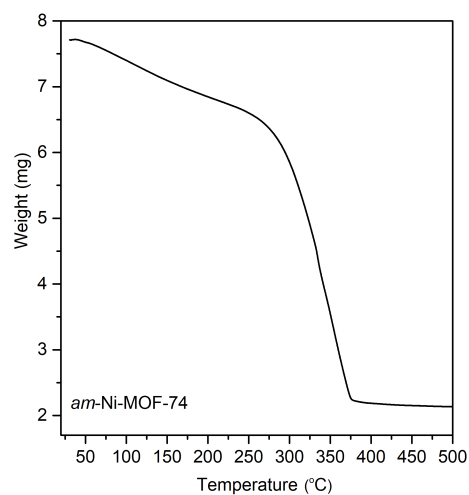


Figure S16: TGA data of *am*-Ni-MOF-74.

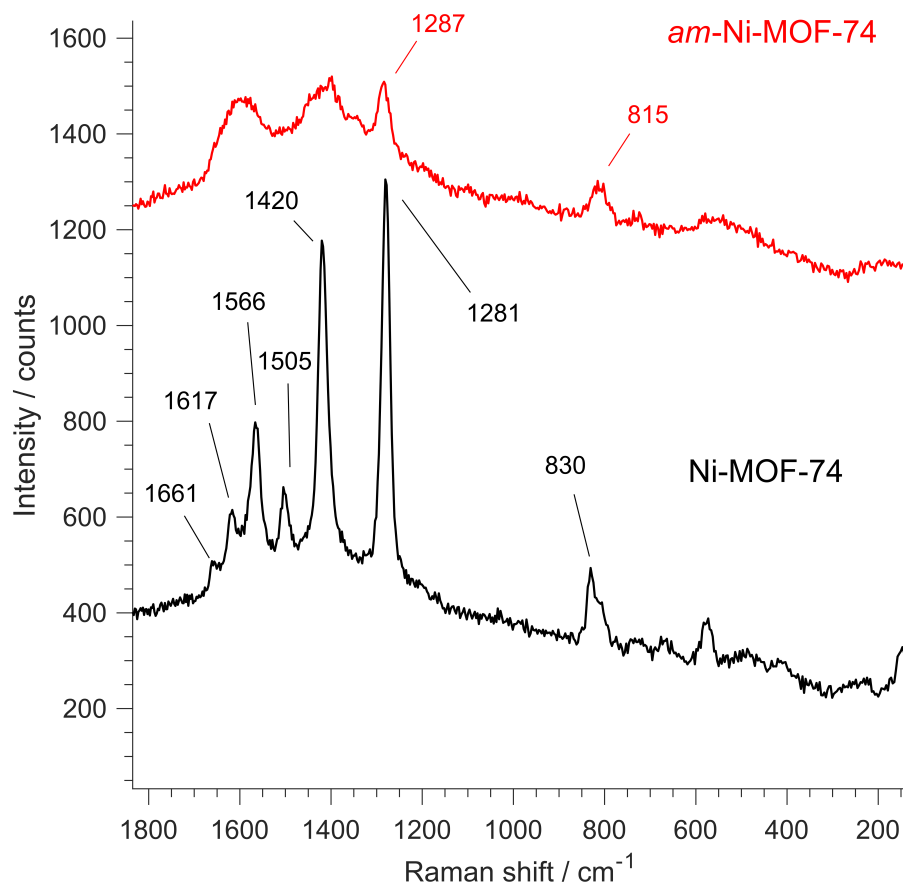


Figure S17: Comparison of *ex situ* Raman spectra of crystalline and amorphous Ni-MOF-74. Raman bands undergoing major changes are highlighted.

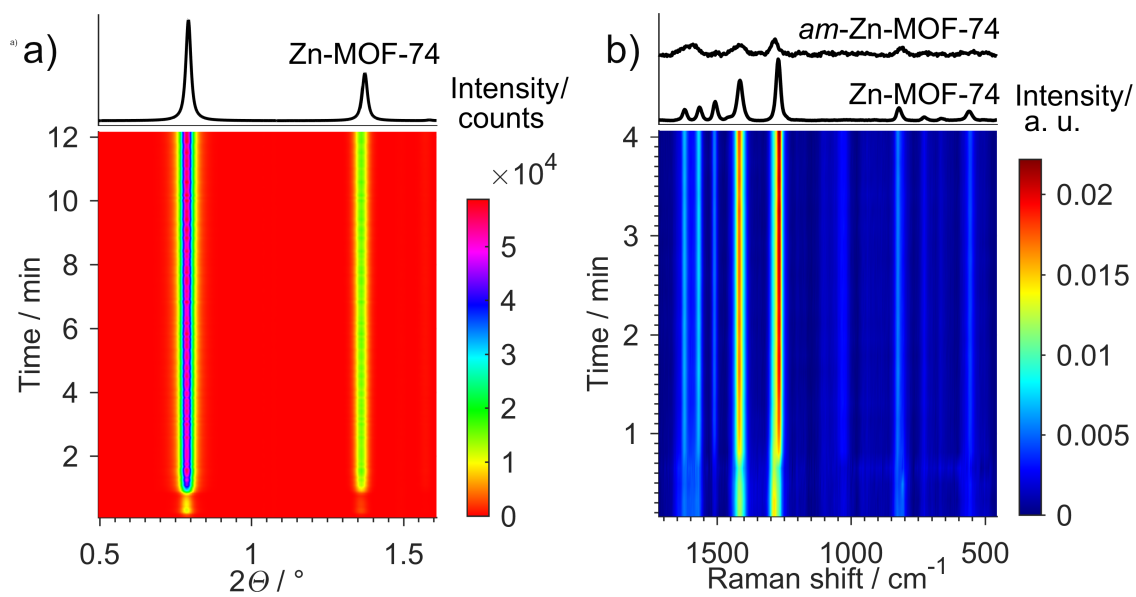


Figure S18: *In situ* monitoring a) PXRD and b) Raman data for recrystallization of Zn-MOF-74 by LAG(MeOH).

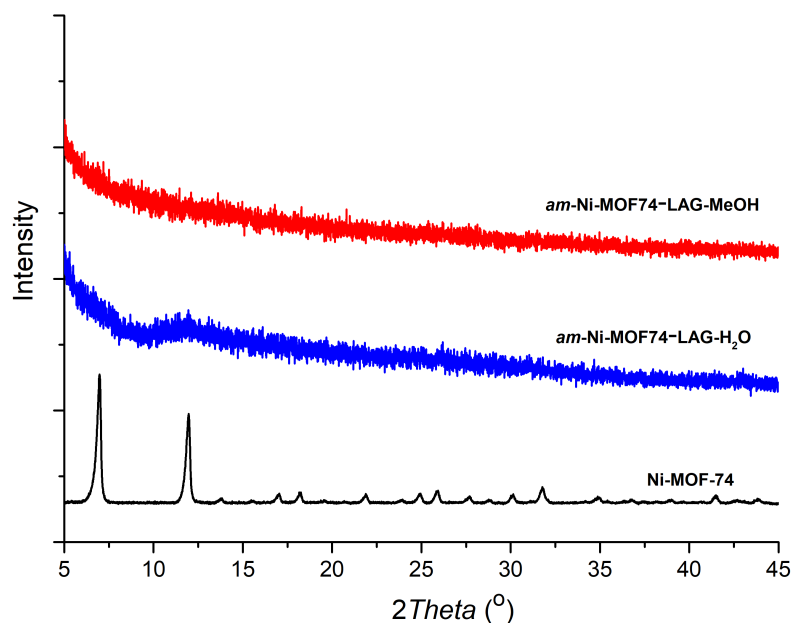


Figure S19: PXRD data for recrystallization of *am*-Ni-MOF-74 by LAG with MeOH (red) and H₂O (blue) compared to the PXRD of crystalline Ni-MOF-74 (black)

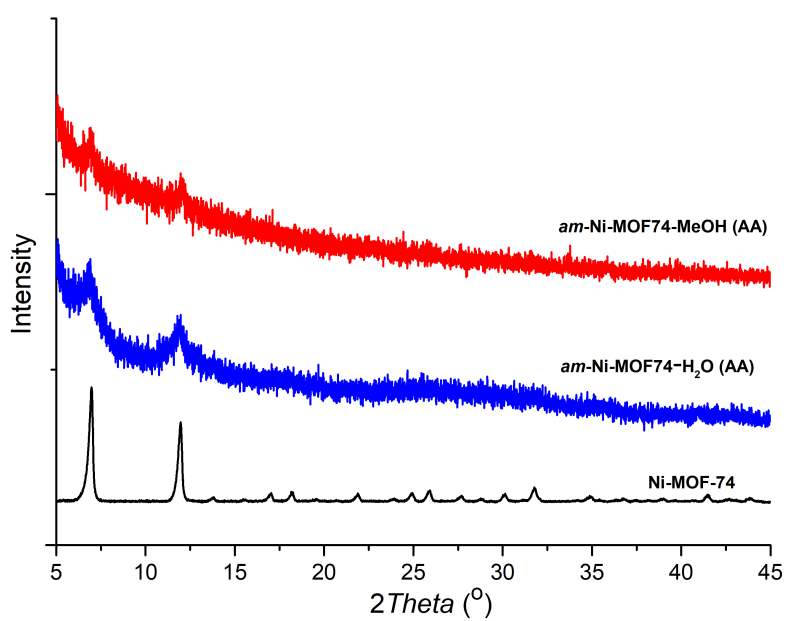


Figure S20: PXRD data for recrystallization of *am*-Ni-MOF-74 by accelerated aging (AA) (10 days at 45°C) in the atmosphere of MeOH (red) and H₂O (blue) compared to the PXRD of crystalline Ni-MOF-74 (black)

References

- [1] G. Ayoub, B. Karadeniz, A. J. Howarth, O. K. Farha, I. Đilović, L. S. Germann, R. E. Dinnebier, K. Užarević and T. Friščić, *Chem. Mater.*, 2019, **31**, 5494–5501.
- [2] S. Cadot, L. Veyre, D. Luneau, D. Farrusseng and E. Alessandra Quadrelli, *J. Mater. Chem. A*, 2014, **2**, 17757–17763.
- [3] S. Lukin, T. Stolar, M. Tireli, M. V. Blanco, D. Babić, T. Friščić, K. Užarević and I. Halasz, *Chem. Eur. J.*, 2017, **23**, 13941.
- [4] S. Lukin, M. Tireli, T. Stolar, D. Barišić, M. V. Blanco, M. di Michiel, K. Užarević and I. Halasz, *J. Am. Chem. Soc.*, 2019, **141**, 1212–1216.
- [5] C. Golze, A. Alfonsov, R. Klingeler, B. Büchner, V. Kataev, C. Mennerich, H.-H. Klauss, M. Goiran, J.-M. Broto, H. Rakoto, S. Demeshko, G. Leibelng and F. Meyer, *Phys. Rev. B*, 2006, **73**, 224403.
- [6] S. Stoll, *EasySpin –EPR spectrum simulation*.
- [7] S. Stoll and A. Schweiger, *J. Magn. Reson.*, 2006, **178**, 42–55.
- [8] J. Krzystek, J.-H. Park, M. W. Meisel, M. A. Hitchman, H. Stratemeier, L.-C. Brunel and J. Telser, *Inorg. Chem.*, 2002, **41**, 4478–4487.
- [9] Y. Krupskaya, A. Alfonsov, A. Parameswaran, V. Kataev, R. Klingeler, G. Steinfeld, N. Beyer, M. Gressenbuch, B. Kersting and B. Büchner, *ChemPhysChem*, 2010, **11**, 1961–1970.
- [10] J. E. Wertz and J. R. Bolton, *Electron Spin Resonances, Elementary Theory and Practical Applications*, McGraw-Hill, New York, 1972.